Remote sensing a low pressure plasma in the radio near field

Seán Kelly[1]* and Patrick J. McNally[1]

[1]*School of Electronic Engineering, Dublin City University, Ireland*

A novel approach to remotely monitor low pressure non-equilibrium plasmas is reported. A magnetic field antenna is positioned in the near field of a capacitively coupled plasma. Magnetic flux from plasma currents, present near the viewport, is intercepted via a calibrated loop antenna placed outside the chamber. The induced signal current is correlated to bulk plasma currents. Comparison of relative harmonic amplitudes show resonance features for lower operating pressures. The geometric resonance and electron-neutral collision frequencies are evaluated from resonant harmonic features. Of particular interest to industrial scenarios, this approach advances remote, non invasive and installation free plasma monitoring.

Plasma diagnosis is central to improving fault detection and control during semiconductor fabrication. Industrial scenarios however present relatively 'hostile' conditions detrimental to immersed probes.[1–3)] Probe contact with the plasma can be disruptive and negatively impact process replication, a key challenge in high volume manufacturing lines. Plasma diagnostics which are non-invasive and installation free (remote) are therefore particularly advantageous for modern industrial plasma scenarios.[4–7)]

Monitoring optical emissions (i.e. optical emission spectroscopy) in a processing plasma is well established.[3,4,8)] To date, however, monitoring of wavelengths emitted in the radio frequency portion of the electromagnetic spectrum from low temperature plasma sources remains relatively unexploited. In this report, a method for measuring and analysis of near field radio emissions in the vicinity of a low pressure non-equilibrium plasma is discussed.

The concept, dubbed Radio Emission Spectroscopy (RES), is illustrated in figure 1. A near field loop antenna (typical diameter ~5-25 mm) intercepts the magnetic flux resulting from currents in proximity to a viewport in the plasma chamber. The loop plane is orientated perpendicular to viewport to intercept currents transiting between the electrodes. A shielded loop antenna design, often used for magnetic field sensing in electromagnetic interference testing, is employed here.[9)] The spatial behaviour of the magnetic field (strictly magnetostatic field) surrounding plasma currents flowing in proximity to the viewport is given by

*E-mail: sean.kelly@dcu.ie

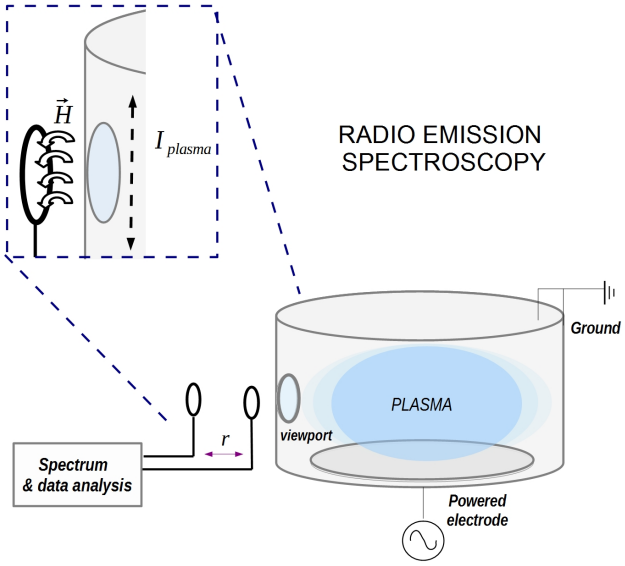

Fig. 1. Setup of near field antenna and signal analysis system (dubbed 'Radio Emission Spectroscopy' RES)

application of the Biot-Savart law.

$$B(r) = \frac{\mu_0}{4\pi} \iiint_V \frac{(J\,dV) \times r}{|r|^3} \tag{1}$$

Here, dV is the volume element for current density J and r represents the separation between the current volume and the antenna position r. The voltage induced in a loop antenna at position r from a nearby magnetic field resulting from plasma currents ($I = J\,dV$) is based on Faraday's induction principle and can be given in the time and frequency domains by the following:

$$V_{loop}(t) = k\frac{\partial I(t)}{\partial t} \tag{2}$$

$$V_{loop}(\omega) = I(\omega) + k(\omega) \tag{3}$$

In equation 3 above, k(ω) represents a frequency dependent correction factor. The calculation of this frequency dependent correction factor between the plasma current and the induced antenna signal enables accurate comparison of the relative magnitudes of current harmonics. This calibration is carried out using a 50 Ω micro-strip transmission line (as a plasma analogue) and a vector network analyser to determine $k(\omega)$ for our custom loop antenna and SMA connector cable. This technique is often employed for H-field loop antenna calibra-

tion in electromagnetic compatibility testing.[10)] Loop designs typically consist of a shielded conductor shorted to the shield with a small gap placed in the conductor loop. At ≈MHz frequencies the electrostatic shielding plays a central role and carries the induced sensing currents.[9)]

Low level signals are analysed using a spectrum analyser with a high dynamic range.[11)] A resolution bandwidth of 100 Hz is sufficient to resolve harmonic peaks. In order to remove ambient radio noise a background scan is performed. This is carried out at a distance sufficiently remote from the plasma (e.g. where the near field signal is completely lost at r > 20 cm in our case) (see figure 2) and subtracted from the near field signal to isolate signals emanating only from the plasma viewport. The low pressure plasma source used here is the Plasma Lab 100 etching system from Oxford Instruments.[12)] More details on this capacitively coupled 13.56 MHz dirven plasma etcher can be found in earlier reports.[13,14)]

Probes to measure voltage and current have previously been incorporated into plasma chamber walls.[15–19)] Signal acquisition is typically carried out via direct sampling (e.g. using an oscilloscope) employing 'direct' analog to digital signal conversion. Radio Frequency (RF) based plasma diagnostics include both interferometry and reflectometry techniques.[20)] These techniques have employed radio approaches utilising heterodyning for signal acquisition[21)] which are flexible with regard to frequency range (not strictly bound to the Nyquist limit) and often allow access to lower signal power levels compared with direct sampling approaches. Recent advances in microprocessor technology have enabled the emergence of 'software defined radio' (SDR) where traditional radio hardware components have been implemented in software. This has lead to recent advances in the flexibility and availability of SDR signal acquisition and spectrum analyser technologies.

The ability to localise the emitted radio signal from the plasma via a near field (magnetic loop) antenna must be emphasised. This resolution ensures that emissions from nearby sources are effectively minimised as the antenna is sensitive to the H-field in the vicinity of the plasma viewport (or alternatively any other non-conductive surface bounding the plasma). In figure 2 (a) we show measurements of the $1/r^3$ dependence of the near H-field close to the viewport (figure 1). Although not shown in figure 2 (a), signals were found to be detectable and discernible from background noise (typically < -70 dBm) at up to r=200 mm in this arrangement (depicted in figure 1). The localised nature of the Radio Emission Spectroscopy (RES) signal corroborates the source of the emission as the plasma over any far field radiation sources which likely includes emissions from nearby plasma chambers, the power unit, match box,

other sections of the transmission line and ambient radio signals. Noise can also be easily removed from the signal in this scenario via an on-line background subtraction at a suitable point away from the near field (see figure 2 (a)). This provides a practical method for signal extraction and is particularly advantageous for implementation in 'radio-noisy' fabrication environments.

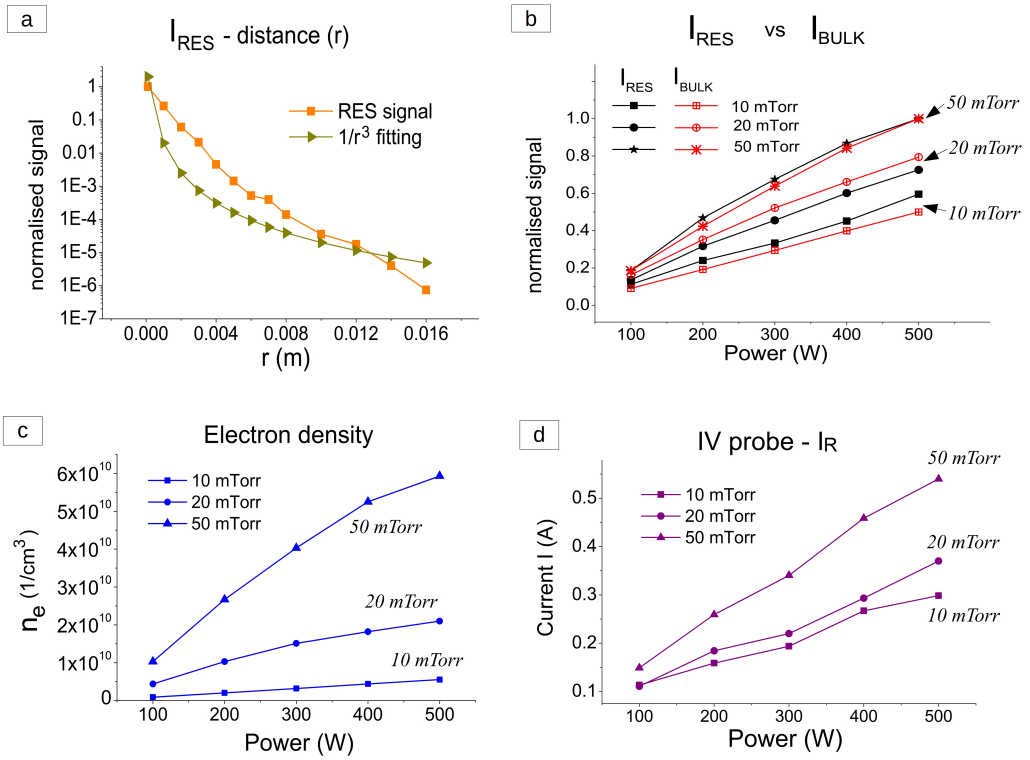

Fig. 2. (a) Distance dependence ('r' in figure 1) of Induced radio signal I_{RES} (dubbed 'Radio Emission Spectroscopy' RES) (b) Comparison of I_{RES} with the bulk plasma current I_{bulk}. (c) Electron density values in centre of discharge using Langmuir probe. (d) Resitive component (I_R) of the total current measured via an in-line an I-V probe

The current in a capacitively coupled plasma (CCP) discharge, driven by rf $E(t) = Re(\hat{E}e^{j\omega t})$, can be given in terms of the plasma dielectric constant ϵ_p.[22)]

$$\nabla \times \hat{H} = -I = j\omega\epsilon_p\hat{E} \tag{4}$$

We consider a circuit analogue for our capacitively coupled plasma which consists of a capacitive sheath in series with an inductive and resistive bulk plasma. The total plasma

permittivity is given by.[2,3,23)]

$$\epsilon_p = \epsilon_0(\frac{1}{s} + \frac{(1-\omega_p^2/(\omega(\omega - j\nu_m))}{1-s}) \tag{5}$$

Here s, the sheath width is normalised to the gap width ($0 < s < 1$), ω_p is the plasma frequency and ν_m is the electron-neutral collision frequency. Inserting ϵ_p into equation 4 above and rearranging as an impedance/admittance relation we find

$$Z^{-1} = \frac{I}{\hat{E}} = \epsilon_0\Bigg(\frac{\omega_p^2\nu_m}{(\omega^2+\nu_m^2)(1-s)} + j\Big(\omega(\frac{\omega_p^2}{\omega^2+\nu_m^2})\frac{1}{(1-s)} - \omega(\frac{1}{s}+\frac{1}{(1-s)})\Big)\Bigg) \tag{6}$$

$$Z^{-1} = \left(\epsilon_0\Big(R - j\Big(\omega L - \frac{1}{\omega C}\Big)\Big)\right)^{-1} \tag{7}$$

Equation 6 has the form of a non-linear RLC circuit impedance shown by equation 7. The well known series (or geometric) resonance frequency $\omega = \omega_g$[3,16,17,23–25)] is given for series resonance condition $\omega L = 1/\omega C$ as

$$\omega_g^2 + \nu_m^2 = s\omega_p^2 \tag{8}$$

The total RES signal is now compared with a calculation of 'bulk' plasma current. We consider the dissipated plasma power using Ohms relation.[3,17,22)]

$$I_{bulk}^2 = P_{diss}\,|Z|^{-1} \tag{9}$$

A 'compressed' or 'summed' variable which takes account of the induced signal strength of the first five harmonics intercepted by our loop antenna, i.e. $I_{RES}^2 = \sum_{n=1}^{5} I_{loop}(\omega_n)^2$ is constructed for comparison to the bulk plasma current. These harmonics are found to typically contain the majority of the induced signal under conditions investigated in this report. By considering only the real portion of the impedance/admittance (i.e. resistance) shown in equation 7 and approximating the width of the plasma bulk $(1-s) \approx 1$ we give a relation between I_{bulk} and induced RES current I_{RES} in terms of electron parameters ω_p and ν_m.

$$I_{RES}^2 = \sum_{n=1}^{k} I_{loop}(\omega_n)^2 \;\propto\; I_{bulk}^2 = P_{diss}\frac{\omega_p^2\nu_m}{(\omega^2+\nu_m^2)} \tag{10}$$

A Langmuir probe[13,14] positioned at the discharge centre is used to measure ω_p (see figure 2 (c)) and the electron temperature T_e. The electron-neutral collision frequency ν_m is calculated using collision cross section data[26] via T_e. Calculated values for ν_m ranged from 38 MHz at 10 mTorr to 104 MHz at 50 mTorr (on average) across the power range. Further, the dissipated power is approximated to be equal to the applied power $P_{diss} = P_{app}$. In figure 2 (b) we see the variation in our compressed variable I_{RES} with comparison to the calculated bulk plasma current I_{bulk}. At a 50 mtorr pressure (O_2 plasma) I_{RES} and I_{bulk} are correlated well over the power range. At lower pressures some deviation occurs (shown in figure 2 (b)). This could be to caused by increased signal noise and/or due to an increase in collision-less heating (which would manifest as an increased reactance) not accounted for in our calculation.

The viewport is located at the equator of our cylindrical plasma chamber. The induced current in our loop antenna is therefore considered to be dominated by currents running in the central portion of the discharge (so called 'bulk' region). This 'bulk' plasma current is typically dominated by the resistive (real part of the impedance) portion of the total current. The total current measured by an inline IV probe[27] (stationed between the matchbox and the powered electrode) was found to decrease with increasing pressure (in contrast to the positive correlation shown in figure 2 (b) and (c)). This total current, however, provides a global (spatially integrated) measurement which includes the current present within the sheaths and the 'bulk' plasma region. A comparison with the 'resistive' component of the current (shown in figure 2 (d)) thus provides a more accurate comparison to the induced RES current and the calculated 'bulk' plasma current. This is accomplished by incorporation of the phase data (which shows decreasing trend with pressure increase) and employment of the relation $I_R = I_{total}\cos(\phi)$ where ϕ is the measured phase. This portion of the total current (shown in figure 2 (d)) correlates positively with both the induced current in the RES signal and the calculated bulk current for increasing pressure.

In order to demonstrate the industrial utility of Radio Emission Spectroscopy (RES) an endpoint experiment using a 4 inch silicon wafer with a spin coated photo-resist film of approx. 2 μm thickness[28] is ashed with an oxygen plasma in our chamber[12] (see figure 3). Measurements of the atomic oxygen (O) 777 nm, 483 nm carbon monoxide (CO) and 656 nm hydrogen (H) emission line intensities[3] are carried out using an optical spectrometer[29] providing corroboration (figure 3 (b)). Endpoint (i.e. total removal of photo-resist layer) occurs as the line intensity of the reaction by-products (i.e. CO 483 nm & H 656 emission lines) falls

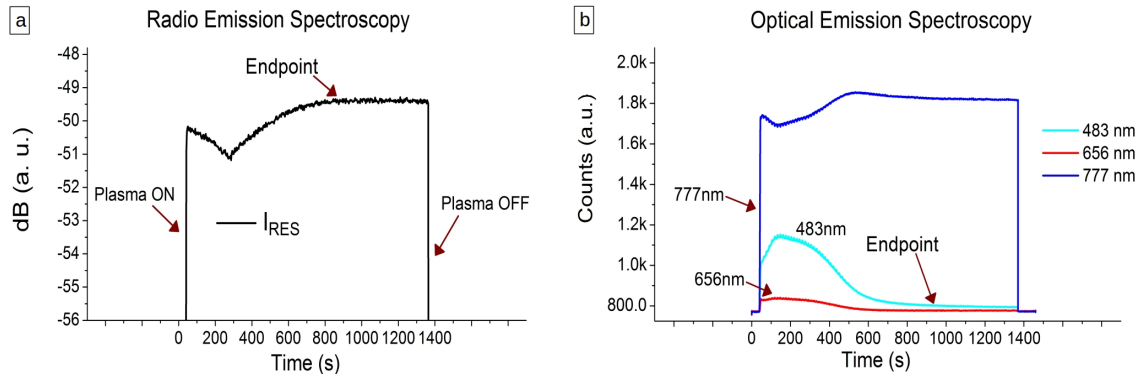

Fig. 3. Industrial utility demonstration: a 100 mm silicon wafer with a spin coated photo-resist of approx. 2 μm thickness[28] is ashed with an Oxygen plasma. (a) & (b): simultaneous measurement of endpoint with Radio Emission Spectroscopy (RES) (I_{RES} includes the summation of 1^{st}-5^{th} harmonics) and Optical Emission Spectroscopy (OES): 777 nm atomic oxygen (O), 483 nm carbon monoxide (CO) & 656 nm hydrogen (H) lines.

off to background levels. This is found to occur after ≈ 900 seconds here which is indicated for both OES and RES (i.e. I_{RES}). As shown in figure 3 the timing of the plasma ignition, endpoint and plasma cessation are correlated in both methods. Differences in the behaviour of each signal can be attributed to the alternate physics of each technique. The 483 nm and 656 nm emission lines monitored show the intensity of reaction by-products in the discharge. The intensity fall off at the process endpoint is therefore a direct proxy for completion of the photo-resist removal from the wafer. The 777 nm emission follows the excitation of atomic oxygen species in the discharge which are consumed during photo-resist removal. At the endpoint a steady state intensity is found providing another proxy for the process completion in this context. The induced current in the RES signal on the other hand follows changes in the bulk plasma current. This shows a (generally) increasing trend as the photo-resist is removed with the signal intensity finally plateauing (similar to the 777 nm optical emission line) to a steady state indicating the process endpoint.

Resonance behaviour in the RES signal harmonics is shown in figure 4 for an oxygen plasma (20 mTorr). Emission is found to occur primarily around narrow bands (≈ Δ100 Hz) located at harmonics of the source driving frequency (13.56 MHz). The occurrence of two distinct geometric resonances is found here. An explanation is offered based on the significant size difference between the two primary sheaths present in the discharge. The oxford instruments plasma lab 100 source (employed in this report) utilises a blocking capacitor to isolate the driven electrode. This results in an asymmetry in the sheath size with a large 'high

voltage' sheath forming over the driven (isolated) electrode, an advantageous arrangement for industrial plasma etchers commonly employed for semiconductor processing applications.[3)] In this context, the grounded sheath width is attributed to the lower frequency geometric resonance and the larger 'high voltage' sheath is correlated to the higher frequency geometric resonance. The sheath asymmetry leads to the two distinct geometric resonances coupled to the current harmonics observed in figure 4.

Damping of the series resonance is due to the electron-neutral collisions given by the frequency ν_m (see equation 8)[3)] and is constrained in the upward direction by the driving frequency ω (i.e. $\nu_m > \omega_{rf}$). Continuing our RLC circuit analogy the series resonance bandwidth (BW) is given by the ratio of the resonant frequency and the Quality or 'Q' factor ω_{geom}/Q where the Q factor is found using the relation X_C/R or X_L/R for the capacitive reactance $X_C = 1/\omega C$ or inductance $X_L = \omega L$. Evaluation via equation 6 leads to the direct relation of the BW to the electron-neutral collision frequency $BW = \nu_m$ which is correlated (see equation 8) to the spreading of the series resonance about ω_g.

A Gaussian distribution is fitted to the upper resonance peaks shown in figure 4. The geometric (ω_g) and electron-neutral collision (ν_m) frequencies are given by the fitted mean ($\omega_g = \mu$) and Full Width at Half Maximum (FWHM) where $BW \approx 2.355\sigma$ (σ = standard deviation) shown in figure 5.

The plasma density/frequency can now be calculated using $\omega_p \approx \sqrt{s}\omega_g$ (equation 8) by extracting the geometric resonance frequency shown in figure 4 and employing an estimate of the total sheath width. A calculation of the high voltage sheath size is carried out by employment of the Child sheath law[22)] coupled with a combination of Langmuir probe measurements[13,14)] for electron density and temperature and I-V measurements for estimation of the sheath voltage.[27)] The 'high voltage' sheath width is estimated here as 0.23 or 23 % of the discharge gap and is found to be approximately static across the power range of interest for conditions shown in figure 2. The upper geometric resonance frequency (shown in figure 4) is selected here and combined with this 'high voltage' sheath width estimation. This gives an electron plasma frequency ranging from 575 MHz at 200 W applied power to 653 MHz at 500 W. If we compare to Langmuir probe measurements preformed at the discharge centre a higher range from 913 MHz at 200 W to 1.3 GHz at 500 W is measured (see figure 2 (c)). A significant spatial variation in the electron plasma frequency/density is however expected between the discharge centre and the region near the viewport.[3)] This density fall-off corroborates the lower plasma frequencies found here from the measured geometric

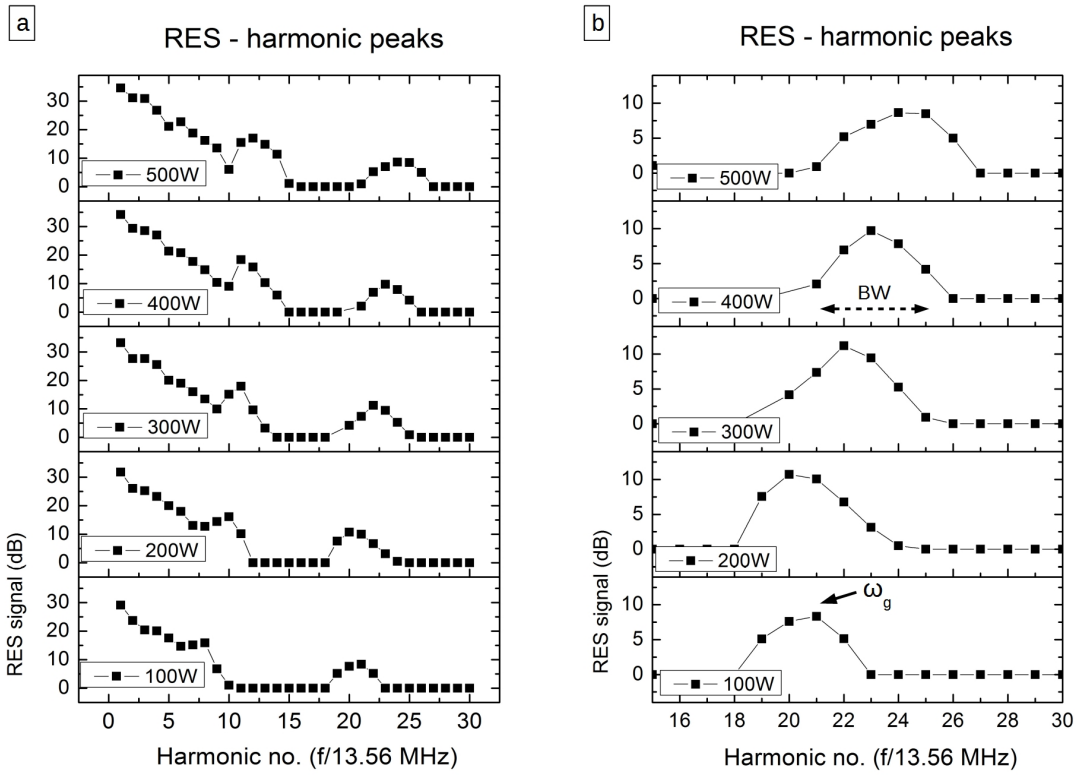

Fig. 4. RES signal frequency analysis: (a) shows relative magnitudes of 1^{st} to 30^{th} harmonic of driving frequency (13.56 MHz). (b) shows the movement of resonance features in higher harmonics for increasing power - extracted plasma parameters are shown in figure 5 below.

frequency ω_g (and our calculated high voltage sheath estimate). Similarly, electron-neutral collision frequency (ν_m) values predicted here were lower compared to those calculated above at the discharge centre. This could be due to lower mean electron energies in the vicinity of the viewport compared to the centre of the discharge which would result in a lower rate of electron-neutral collisions.

Investigations of the radiated (far field) radio signal were also carried out. Results, however, showed limited diagnostic potential with signals (generally) found to be insensitive to plasma parameters. Frequency analysis revealed harmonic peaking at wavelengths of ~0.5-1 meters across a range of applied powers. This insensitivity likely reflects some physical aspect of the transmission line (e.g. chamber diameter) over any correlation to plasma parameters.

In this report we explore the diagnostic potential of a non-invasive magnetic loop antenna placed in the radio field of a low temperature processing plasma. Monitoring of frequencies near the driving frequency are shown to be an effective proxy to monitor current variations in the plasma. This has diagnostic potential as a contact-less sensor for endpoint detection

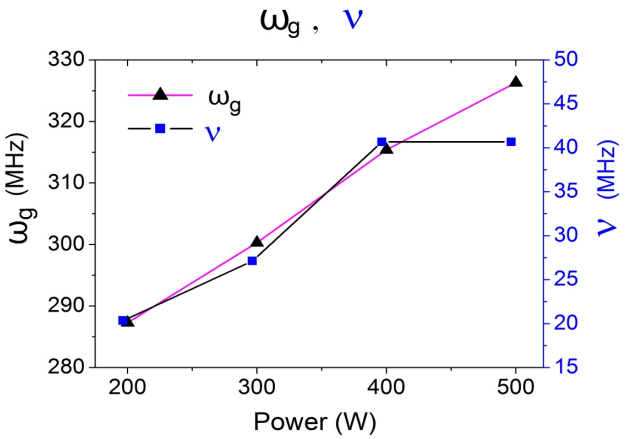

Fig. 5. Extracted values of the series resonance (ω_g) and electron-neutral collision frequencies (ν) from harmonic resonance peaks shown in figure 4.

(e.g. optical emission failure due to window coating) and for identification of arcing, pump or matching failure events, common 'nuisance events' in fabrication scenarios.

Frequency analysis of the higher harmonics present in the near field signal at lower operating pressures showed resonance behaviour which is linked to fundamental plasma parameters. Extraction of the series (or geometric) plasma and electron-neutral collision frequencies is demonstrated for an oxygen plasma.

Acknowledgment: This work is funded by Enterprise Ireland grant no. CF2014-4300. SK and PMN would like to thank Conor Murphy for his technical assistance. SK would like to thank Mr. Sharath Kumar for assistance with the Langmuir probe system and Dr. Cezar Gaman for helpful discussions on the topic.

References

1) R. Shul and S. Pearton, *Handbook of Advanced Plasma Processing Techniques* (Springer Berlin Heidelberg, 2011),
URL: https://books.google.ie/books?id=D_bsCAAAQBAJ

2) P. Chabert and N. Braithwaite, *Physics of Radio-Frequency Plasmas* (Cambridge University Press, 2011),
URL: https://books.google.ie/books?id=oB03j-bbNXcC

3) G. Franz, *Low Pressure Plasmas and Microstructuring Technology*, SpringerLink: Springer e-Books (Springer Berlin Heidelberg, 2009),
URL: https://books.google.ie/books?id=Uhj9zjYZ458C

4) V. M. Donnelly and A. Kornblit, *Plasma etching: Yesterday, today, and tomorrow*, Journal of Vacuum Science & Technology A: Vacuum, Surfaces, and Films **31** (2013) (5), p. 050825,
URL: http://dx.doi.org/10.1116/1.4819316

5) S. Samukawa, M. Hori, S. Rauf, K. Tachibana, P. Bruggeman, G. Kroesen, J. C. Whitehead, A. B. Murphy, A. F. Gutsol, S. Starikovskaia, U. Kortshagen, J.-P. Boeuf, T. J. Sommerer, M. J. Kushner, U. Czarnetzki and N. Mason, *The 2012 Plasma Roadmap*, Journal of Physics D: Applied Physics **45** (2012) (25), p. 253001,
URL: http://stacks.iop.org/0022-3727/45/i=25/a=253001

6) P. J. Bruggeman and U. Czarnetzki, *Retrospective on ‘The 2012 Plasma Roadmap’*, Journal of Physics D: Applied Physics **49** (2016) (43), p. 431001,
URL: http://stacks.iop.org/0022-3727/49/i=43/a=431001

7) M. B. Hopkins and J. F. Lawler, *Plasma diagnostics in industry*, Plasma Physics and Controlled Fusion **42** (2000) (12B), p. B189,
URL: http://stacks.iop.org/0741-3335/42/i=12B/a=314

8) I. Herman, *Optical Diagnostics for Thin Film Processing* (Elsevier Science, 1996),
URL: https://books.google.ie/books?id=ozzufyn7brQC

9) C. F. Carobbi, L. Millanta and L. Chiosi, *The high-frequency behavior of the shield in the magnetic-field probes*, in *Electromagnetic Compatibility, 2000. IEEE International Symposium on* (IEEE, 2000), vol. 1, pp. 35–40

10) International Electrotechnical Commission (IEC) directive, *International Electrotechnical Commission (IEC) directive* (2017),
URL: http://www.iec.ch/

11) Tektronix RSA306 real time signal analyser, *Tektronix UK Ltd.*
URL: http://www.tek.com/

12) Oxford Instruments Ltd., *Oxford Instruments Plasma Lab 100* (2017),
URL: http://www.oxfordplasma.de/systems/100ll.htm

13) S. Kechkar, P. Swift, S. Kelly, S. Kumar, S. Daniels and M. Turner, *Investigation of the electron kinetics in O 2 capacitively coupled plasma with the use of a Langmuir probe*, Plasma Sources Science and Technology **26** (2017) (6), p. 065009,
URL: http://stacks.iop.org/0963-0252/26/i=6/a=065009

14) S. Kechkar, P. Swift, J. Conway, M. Turner and S. Daniels, *Investigation of atomic oxygen density in a capacitively coupled O_2 /SF_6 discharge using two-photon absorption laser-induced fluorescence spectroscopy and a Langmuir probe*, Plasma Sources Science and Technology **22** (2013) (4), p. 045013,
URL: http://stacks.iop.org/0963-0252/22/i=4/a=045013

15) R. Baude, F. Gaboriau and G. Hagelaar, *Wall current probe: A non-invasive in situ plasma diagnostic for space and time resolved current density distribution measurement*, Review of Scientific Instruments **84** (2013) (8), p. 083502

16) E. Semmler, P. Awakowicz and A. von Keudell, *Heating of a dual frequency capacitively coupled plasma via the plasma series resonance*, Plasma Sources Science and Technology **16** (2007) (4), p. 839,
URL: http://stacks.iop.org/0963-0252/16/i=4/a=020

17) M. Klick, W. Rehak and M. Kammeyer, *Plasma Diagnostics in rf Discharges Using Nonlinear and Resonance Effects*, Japanese Journal of Applied Physics **36** (1997) (7S), p. 4625,
URL: http://stacks.iop.org/1347-4065/36/i=7S/a=4625

18) K. H. Baek, E. Lee, M. Klick and R. Rothe, *Comprehensive understanding of chamber conditioning effects on plasma characteristics in an advanced capacitively coupled plasma etcher*, Journal of Vacuum Science & Technology A: Vacuum, Surfaces, and Films **35** (2017) (2), p. 021304

19) S. Rauf and M. J. Kushner, *Diagnostic technique for measuring plasma parameters near surfaces in radio frequency discharges*, Applied Physics Letters **73** (1998) (19), pp. 2730–2732,
URL: http://dx.doi.org/10.1063/1.122572

20) H. J. Hartfuss, *RF techniques in plasma diagnostics*, Plasma Physics and Controlled Fusion **40** (1998) (8A), p. A231,

URL: http://stacks.iop.org/0741-3335/40/i=8A/a=016

21) H. J. Hartfuss, T. Geist and M. Hirsch, *Heterodyne methods in millimetre wave plasma diagnostics with applications to ECE, interferometry and reflectometry*, Plasma Physics and Controlled Fusion **39** (1997) (11), p. 1693,
URL: http://stacks.iop.org/0741-3335/39/i=11/a=001

22) M. Lieberman and A. Lichtenberg, *Principles of Plasma Discharges and Materials Processing* (Wiley, 2005),
URL: https://books.google.ie/books?id=m0iOga2XE5wC

23) B. P. Wood, M. A. Lieberman and A. J. Lichtenberg, *Sheath motion in a capacitively coupled radio frequency discharge*, IEEE Transactions on Plasma Science **19** (1991) (4), pp. 619–627

24) J. Taillet, *Resonance-Sustained Radio Frequency Discharges*, American Journal of Physics **37** (1969) (4), pp. 423–441,
URL: http://dx.doi.org/10.1119/1.1975598

25) S. Wilczek, J. Trieschmann, D. Eremin, R. P. Brinkmann, J. Schulze, E. Schuengel, A. Derzsi, I. Korolov, P. Hartmann, Z. Donk and T. Mussenbrock, *Kinetic interpretation of resonance phenomena in low pressure capacitively coupled radio frequency plasmas*, Physics of Plasmas **23** (2016) (6), p. 063514,
URL: http://dx.doi.org/10.1063/1.4953432

26) LXcat, *electron scattering database http://www.lxcat.laplace.univ-tlse.fr/database.php: Cross sections extracted from PROGRAM MAGBOLTZ, VERSION 7.1 JUNE 2004* (2017)

27) Impedans Ltd., *Octiv Poly I-V probe from Impedans Ltd.* (2017),
URL: https://www.impedans.com/octiv-poly

28) B. Keville, C. Gaman, Y. Zhang, A. M. Holohan, M. M. Turner and S. Daniels, *Attenuation of wall disturbances in an electron cyclotron resonance oxygenargon plasma using real time control*, Journal of Vacuum Science & Technology A: Vacuum, Surfaces, and Films **32** (2014) (4), p. 041301,
URL: http://dx.doi.org/10.1116/1.4879458

29) Ocean Optics, HR 1000 Optical Emission Spectrometer, *Ocean Optics Ltd.* (2017),
URL: http://www.oceanoptics.com